Available online at www.sciencedirect.com
SCIENCE DIRECT®
Journal of Computational Physics 192 (2003) 624–642
JOURNAL OF COMPUTATIONAL PHYSICS
www.elsevier.com/locate/jcp

Numerical simulation of wavy falling film flow using VOF method

D. Gao *, N.B. Morley, V. Dhir

Department of Mechanical and Aerospace Engineering, University of California, Los Angeles, CA 90095, USA

Received 9 January 2003; received in revised form 31 July 2003; accepted 31 July 2003

Abstract

Surface wave dynamics of vertical falling films under monochromatic-frequency flowrate-forcing perturbations is computed by the direct simulation of Navier–Stokes equations using the Volume of Fluid (VOF) method to track free surfaces and the Continuum Surface Force (CSF) model to account for dynamic boundary conditions at free surfaces. The numerical VOF–CSF model is completely formulated, and more attention is given to understanding instabilities of thin films. At low frequency and high flowrate, the small inlet disturbance develops into large solitary waves preceded by small capillary bow waves. The circulation flow compatible with the solitary wave size is observed in the solitary peak. On the other hand, at high frequency and low *Re*, small-amplitude waves in nearly sinusoidal shape without forerunning capillary waves are formed on the surface. The quasi-periodic waveforms are found to occur at the nearly sinusoidal wave regime. The slight increase in wave-amplitude and wavelength, and decrease in residual thickness as waves evolves downstream are observed for both solitary waves and sinusoidal types. The variation of velocity and pressure along a wave are strong at the wave trough and capillary wave region, due to the large surface curvature there. The pressure variation perpendicular to the wall is negligible and only a small variation is observed at the solitary wave trough and capillary region.

1. Introduction

Surface wave evolution on a thin film falling down an inclined or vertical surface exhibits a rich variety of wave dynamics, and thus has attracted the attention of many researchers. As summarized in the recent review by Chang [1] and the comprehensive study by Liu and Gollub [2], well-characterized periodic surface waves occur at a low to medium region of flowrate ($Re < 200$). The thin film flow is unstable to long-wave disturbances, and the instability is dominated by gravity, viscosity and surface tension effects.

Yih [3] was the first to formulate linear instability from infinitesimal long-wave disturbances and give the instability condition

* Corresponding author. Tel.: 1-310-206-4805; fax: 1-310-825-2599.
E-mail address: donghong@seas.ucla.edu (D. Gao).

0021-9991/$ - see front matter © 2003 Elsevier B.V. All rights reserved.
doi:10.1016/j.jcp.2003.07.013

$$\frac{6Re}{5} - \cot\beta - \alpha^2 \frac{1}{3} We\, Re > 0. \tag{1}$$

Here, β is the inclination angle to the horizontal and α is the wavenumber. Re is based on the average velocity u_* and thickness h_* of the corresponding flat film, and $We = \sigma/\rho u_*^2 h_*$ with σ the surface tension and ρ the mass density. If wavelengths are substantially long, the above equation reduces to the most often cited relation $Re_c = (6/5)\cot\beta$. The linear-wave velocity at onset is 3. In another form of the linear solution, the cut-off frequency is

$$F_c = \frac{3}{2\pi}\sqrt{\frac{6/5Re - \cot\beta}{1/3Re\, We}} = \frac{3}{\pi}\sqrt{\frac{9}{10}\frac{Re - Re_c}{Re\, We}} \tag{2}$$

which has been recently verified experimentally by Liu and co-workers [2,4]. After the onset of instability, the exponential growth is rapidly arrested by nonlinear effects, and steady finite-amplitude sinusoidal waves or large-amplitude solitary waves are formed within a frequency range. The nonlinear dynamics was investigated by weakly nonlinear theories [5,6], and recently by advanced nonlinear theories [1,7] based on the boundary layer equations.

Since the pioneering experiment by Kapitza and Kapitza [8] in 1949, extensive experimental studies of wavy thin films have been done by Krantz and Goren [9] in the early 1970s, and Alekseenko et al. [10] in the 1980s, and recently by Nosoko et al. [11], Liu and Gollub [2] and Liu et al. [12]. The work of Krantz and Goren [9], where the Re number is less than or about 1, is essentially limited to the linear region. The Kapitza and Kapitza [8] flows are in the range of $7 < Re < 23$, and the Nosoko et al. [11] experiment spans a wide range $15 < Re < 90$. Kapitzas [8], Alekseenko et al. and Nosoko et al. all have observed small-amplitude sinusoidal waves and large-amplitude solitary waves with fore-running capillary waves. Nosoko et al. [11] provided an empirical equation relating the wave traveling velocity to flowrate, surface tension and forcing perturbation frequency for the steady-state waves on vertical films. Alekseenko et al. [10] did velocity profile measurements and analyzed the variation of velocity profiles from the parabolic one for sinusoidal-type and solitary-type waves.

The experiments performed by Liu and co-workers [2,12] are on inclined films with a small angle to the horizontal (4–10°), and thus they were able to observe closely the whole evolution process of a small inlet perturbation. In the work of Liu and Gollub [2] it took about 150 cm running length to obtain steady-state periodic waves, whereas on falling films [8,10,11] it was just 10–30 cm. Liu and Gollub [2] gave a comprehensive picture to show the frequency ranges in which finite-amplitude sinusoidal waves, large-amplitude solitary waves, and sideband and subharmonic secondary instabilities appear, respectively. The later work of Liu et al. [12] was focused on the transition from well-developed 2-D waves to 3-D waves, in which the transitional instability was divided into synchronous mode and the herringbone pattern. Liu and co-workers [2,12] also performed systematic analyses of solitary wave dynamics and provided valuable suggestions and information to future nonlinear theoretical treatments.

Although experimental evidence indicates that a 2-D regular wave pattern can result from a natural disturbance [8,11] or periodic forcing disturbance, apparently it is difficult to obtain such a regular wavy surface without periodic forcing, especially on a film with a small inclination angle. Indeed, Liu and Gollub [2] pointed out that regular waves do not appear on their inclined films without forcing. All of the aforementioned studies employ forcing disturbances. Krantz and Goren used wire vibrations submerged in the film to generate waves. The Kapitza and Kapitza [8], Alekseenko et al. [10], Nosoko et al. [11] and Liu and co-workers [2,12] excited the waves by pulsations of liquid flowrate. These experiments show that the evolution of 2-D waves and the resulted steady-state wave shapes are strongly dependent on forcing frequencies. For a given Re, large solitary waves, which have a very steep front and fore-running capillary waves, appear at low frequencies, while finite-amplitude sinusoidal waves are present at high frequencies.

Wavy film flow is a challenge both for experimental measurement and for numerical simulation due to the typical length scales: a few millimeters thickness, but tens to hundreds centimeters running length to exhibit wave characters. Thanks to numerous available experimental and theoretical studies, wavy film flows under high viscosity and surface tension effects also serve as good examples for the validation of a numerical scheme for simulating free-surface flows. The direct numerical study can offer further insights into thin film instability that are not easily obtained from experiments. There are some pertinent computations using Finite-Element Methods (FEM), such as Ho and Patera [13], Malamataris and Papanastasiou [14], Salamon et al. [15], Ramaswamy et al. [16] and Krishnamoorthy et al. [17]. Malamataris et al. focused on a modified outflow boundary condition by calculating traveling waves in truncated domains. Salamon et al. [15] assumed an initial sinusoidal waveform, and solved the governing equations in the reference frame moving with the wave. Ramaswamy et al. [16] and Krishnamoorthy et al. [17] used the so-called Arbitrary Eulerian–Lagrangian method, where a grid velocity (w^x, w^y) must be judiciously selected in order to handle very large deformations. The moving surface was captured by a Lagrangian-type method (spine). The computations made by Ho and Patera [13], Salamon et al. [15], Ramaswamy et al. [16] and Krishnamoorthy et al. [17] introduced spatial waves on initial films and used periodic boundary conditions with the constraint that the mean film thickness is conserved. This is not compatible with the experimental conditions corresponding obviously to an open flow condition where the flowrate is conserved. Indeed, both Kapitza and Kapitza [8] and Alekseenko et al. [10] reported a decrease of the average film downstream.

It is desired to simulate film flow under an inlet flowrate perturbation and investigate the response to the small monochromatic forcing disturbance. The computational film running length must be long enough to allow the inlet disturbance to evolve into steady-state periodic waves, and thus a vertical film is often the choice for such computations. Here we use the Volume of Fluid (VOF) surface tracking method [18–20] based on the finite volume idea, and the Continuum Surface Force (CSF) model [19,21] to account for the surface tension effect. Different from the above-mentioned numerical method, the present numerical scheme is based on a fixed staggered grid. We do not need to assume a prior waveform and velocity, and to re-formulate the equations in a moving frame. The method is general to any kinds of free-surface flows. There is no special treatment for the wavy film flows. We will present the simulation results and compare the results with the corresponding experimental data for selected characteristic terms, and provide further analysis and discussion in conjunction with what we have already known about thin film instability. To be consistent with most research on this topic, the results are presented in the dimensionless system with the flat film height and average velocity as the scaling values.

2. Governing equations

We consider a two-dimensional thin film flow on an inclined plane at angle β to the horizontal. The x-axis is oriented streamwise along the plane. The y-axis is perpendicular to the plane in the film thickness direction with the origin at the liquid-plane interface. The flow is considered to be a laminar incompressible Newtonian and isothermal flow with velocity field $\mathbf{V} = (u, v)$, and governed by the Navier–Stokes equations and continuity equation as:

$$\frac{\partial u}{\partial t} + u\frac{\partial u}{\partial x} + v\frac{\partial u}{\partial y} = -\frac{\partial p}{\partial x} + \frac{1}{Re}\nabla^2 u + \frac{1}{Fr^2}\sin\beta, \tag{3}$$

$$\frac{\partial v}{\partial t} + u\frac{\partial v}{\partial x} + v\frac{\partial v}{\partial y} = -\frac{\partial p}{\partial y} + \frac{1}{Re}\nabla^2 v - \frac{1}{Fr^2}\cos\beta, \tag{4}$$

$$\frac{\partial u}{\partial x}+\frac{\partial v}{\partial y}=0, \tag{5}$$

where the characteristic length and velocity are chosen to be the corresponding flat film thickness h_* and average velocity u_*. The time t is normalized by h_*/u_* and pressure p by ρu_*^2, with ρ the mass density of liquid. The dimensionless parameters: Reynolds (*Re*), Froude (*Fr*) and Weber (*We*) are defined as

$$Re=\frac{u_* h_*}{v}, \quad Fr^2=\frac{u_*^2}{g h_*}, \quad We=\frac{\sigma}{\rho u_*^2 h_*}, \tag{6}$$

where v is the kinematic viscosity of liquid, g the gravity, and σ the surface tension. The velocity profile and average velocity of the fully developed flat film are

$$u=\frac{3}{2}(2y-y^2), \quad u_*=\frac{g h_*^2 \sin\beta}{3v}. \tag{7}$$

Due to the normalization by the flat film, we have $Fr^2=Re/3$.

The boundary conditions on the bottom wall are the non-slip condition and the lack of liquid flowing into and out-of the plane, as formulated

$$u=v=0 \quad \text{at } y=0. \tag{8}$$

As the liquid drains downstream, the film thickness $h(x,t)$ varies with the streamwise distance and time. The interface location is associated with the local velocity by the kinematic condition

$$v=\frac{\partial h}{\partial t}+u\frac{\partial h}{\partial x} \quad \text{at } y=h. \tag{9}$$

At a free surface, the normal stress is balanced by the capillary force and the shear stress vanishes for the constant property flow. The dynamic conditions at an interface can be written as

$$-\mathbf{T}\cdot\hat{\mathbf{n}}\cdot\hat{\mathbf{n}}-p_{\text{gas}}=\kappa We \quad \text{at } y=h, \tag{10}$$

where $\mathbf{T}=-p\mathbf{I}+(\nabla\mathbf{V}+(\nabla\mathbf{V})^{\mathrm{T}})/Re$ is the stress tensor with $\mathbf{I}$ the identity tensor, $\kappa=-\partial^2 h/\partial x^2[1+(\partial h/\partial x)^2]^{-3/2}$ is the curvature of the interface, $\hat{\mathbf{n}}=(-\partial h/\partial x,1)[1+(\partial h/\partial x)^2]^{-1/2}$ is the unit outward normal vector.

3. Numerical methods and conditions

The numerical simulation of free-surface flows composed of two immiscible fluids involves two coupled tasks: (1) resolving the flow field and (2) updating the position of the interface. The first task is completed by solving the Navier–Stokes equations. It is numerically implemented via the projection method, where an intermediate velocity field is first determined from the diffusion–convection equations without regard to the pressure term, and then the pressure is decoupled from the momentum equations to construct the Pressure Poisson Equation (PPE). In the second step, the PPE is solved and the pressure field is used to correct the preliminary velocity prediction, thus recovering the continuity constraint. The second task is carried out via the Volume of Fluid (VOF) method [18–20]. The VOF method actually keeps and updates the field of volume fraction of one fluid in each cell instead of surface height. The advantage of the VOF method is that there is no topological constraint. Thus, the VOF method has been widely used to track the interface of two immiscible fluids, such as water and air. In the present work, the one-fluid model (where gas phase dynamics is ignored) is implemented in the code for computations. Sometimes the one-flow model is also

termed the void model because the gas phase is often assumed void. The surface tension is taken into account through the Continuum Surface Force (CSF) model [19,21], where the surface force is transformed to a body force $\mathbf{F}_{sv}$ which is only non-zero in the limited thickness interface region. The scalar f is used to denote the volume fraction field also called VOF field. Therefore, the governing equations for the one-fluid VOF–CSF model include the Navier–Stokes equations, continuity equation and VOF advection equation. They are written as:

$$\frac{\partial \mathbf{V}}{\partial t} + (\mathbf{V}\cdot\nabla)\mathbf{V} = \frac{\rho_l}{\bar{\rho}}\left[-\nabla p + \frac{1}{Re}\nabla\cdot\left(\frac{\bar{\mu}}{\mu_l}\tau\right) + F_{sv}\right] + \frac{1}{Fr^2}\hat{\mathbf{g}}, \tag{11}$$

$$\nabla\cdot\mathbf{V} = 0, \tag{12}$$

$$\frac{\partial f}{\partial t} + \nabla\cdot(f\mathbf{V}) - f\nabla\cdot\mathbf{V} = 0, \tag{13}$$

where $\hat{\mathbf{g}} = (\sin\beta, -\cos\beta)$ is the unit gravity vector and τ is the viscous stress tensor. The VOF advection equation (13) appears in the conservative form adopted from Puckett et al. [22]. The dimensionless governing equations indicate that besides liquid properties, the gas properties are also required to obtain the localized $\bar{\rho}$, $\bar{\mu}$ by the volume weighted average of two liquids as

$$\bar{\rho} = f\rho_l + (1-f)\rho_g, \quad \bar{\mu} = f\mu_l + (1-f)\mu_g, \tag{14}$$

where the subscript l denotes liquid and the subscript g denotes gas.

During the numerical solution process, we apply the free-surface boundary conditions. There are three hydrodynamic boundary conditions at free surfaces: normal stress balance, tangential stress balance, and the kinematic equation. The kinematic condition is implied by the VOF advection. The dynamics stress balance is realized through the CSF model incorporated in the momentum equations by introducing a volume force $\mathbf{F}_{sv}$. The localized volume force $\mathbf{F}_{sv}$ is calculated from the volume fraction data by

$$\mathbf{F}_{sv} = We\kappa\nabla f, \tag{15}$$

where κ is the curvature of surface. The interface characteristic parameters, the outward normal vector $\mathbf{n}$ and curvature κ, are calculated as

$$\mathbf{n} = (n_x, n_y) = -\nabla f, \quad \hat{\mathbf{n}} = \mathbf{n}/|\mathbf{n}|, \tag{16}$$

$$\begin{aligned}\kappa = (\nabla\cdot\hat{\mathbf{n}}) &= -\frac{1}{|\mathbf{n}|}\left[\left(\frac{\mathbf{n}}{|\mathbf{n}|}\cdot\nabla\right)|\mathbf{n}| - (\nabla\cdot\mathbf{n})\right] \\ &= -\frac{1}{|\mathbf{n}|}\left[\frac{n_x^2}{|\mathbf{n}|^2}\frac{\partial n_x}{\partial x} + \frac{n_x n_y}{|\mathbf{n}|^2}\left(\frac{\partial n_x}{\partial y} + \frac{\partial n_y}{\partial x}\right) + \frac{n_y^2}{|\mathbf{n}|^2}\frac{\partial n_y}{\partial y} - \frac{\partial n_x}{\partial x} - \frac{\partial n_y}{\partial y}\right].\end{aligned} \tag{17}$$

The VOF method involves a lot of details during solving VOF advection, or say, updating VOF data. The split-operator method [22] is used for VOF advection. As indicated by its name, a split algorithm first moves the fluid at one component of the velocity and obtains an intermediate VOF field, and then moves the fluid at the other component of the velocity and obtains the final VOF data. By this idea, Eq. (13) is split to:

$$\frac{\partial f}{\partial t} + \frac{\partial(fu)}{\partial x} = f\frac{\partial u}{\partial x}, \tag{18}$$

$$\frac{\partial f}{\partial t}+\frac{\partial (fv)}{\partial y}=f\frac{\partial v}{\partial y}. \tag{19}$$

Discretizing f implicitly on the right-hand side of Eq. (18) and explicitly on the right-hand side of Eq. (19), we obtain the finite difference operator-split VOF advection equation

$$f^{*}_{i,j}=\left[f^{n}_{i,j}-\frac{\Delta t}{\Delta x}(F_{i+1/2,j}-F_{i-1/2,j})\right]\Big/\left[1-\frac{\Delta t}{\Delta x}(u_{i+1/2,j}-u_{i-1/2,j})\right], \tag{20}$$

$$f^{n+1}_{i,j}=f^{*}_{i,j}\left[1+\frac{\Delta t}{\Delta y}(v_{i,j+1/2}-v_{i,j-1/2})\right]-\frac{\Delta t}{\Delta y}(G^{*}_{i,j+1/2}-G^{*}_{i,j-1/2}), \tag{21}$$

where $F_{i+1/2,j}$ denotes the x-flux of the liquid across the right face of cell (i,j) in Δt and $G_{i,j+1/2}$ denotes the y-flux of the liquid across the top face. Near a free surface as illustrated in Fig. 1, only the dark area inside the rectangular area with width $u_{i+1/2,j}\Delta t$ and height Δy_j, not the whole rectangular, will cross the right face and enter the $(i+1,j)$ cell in the Δt interval. The flux $F_{i+1/2,j}$ is decided by

$$F_{i+1/2,j}=V_{i+1/2,j}/(\Delta t\Delta y_j), \tag{22}$$

where the volume $V_{i+1/2,j}$ is determined from the free surface geometry.

The surface configuration is required by VOF advection to maintain mass conservation, namely to calculate the $V_{i+1/2,j}$ in the above specific case. Here, a surface is constructed as segment lines in local cell coordinates from the VOF data of the previous time step. The VOF method usually consists of two parts: an interface reconstruction algorithm to determine the interface and a VOF advection algorithm to update the volume fraction data. A surface line can be determined by the normal vector and the interception length with the local y-axis. For example, for the cell (i,j) as shown in Fig. 2, the surface is represented by the line function $y=k_{i,j}x+d_{i,j}$. The slope is obtained from the normal vector $\mathbf{n}_{i,j}$ by $k_{i,j}=-[n_x/n_y]_{i,j}$. The intersection point of the line with the local y-axis is determined by the volume of liquid in the cell and the slope. Specifically for the case of $0<k_{i,j}<\Delta y_j/\Delta x_i$ and $V_{i,j}<|k_{i,j}|\Delta x_i^2/2$, the value $d_{i,j}$ given by

$$d_{i,j}=-\left(\Delta y_j/2-(2kV)^{1/2}_{i,j}+k_{i,j}\Delta x_i/2\right). \tag{23}$$

Other cases at the different fluid occupation conditions can be computed in a similar way.

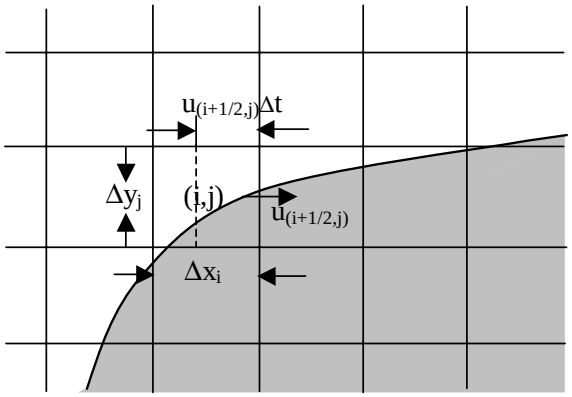

Fig. 1. The x-flux calculation in the VOF split advection algorithm. Only the volume of the dark fluid at the right of the dotted line in the cell (i,j) crosses the right face of the cell in Δt.

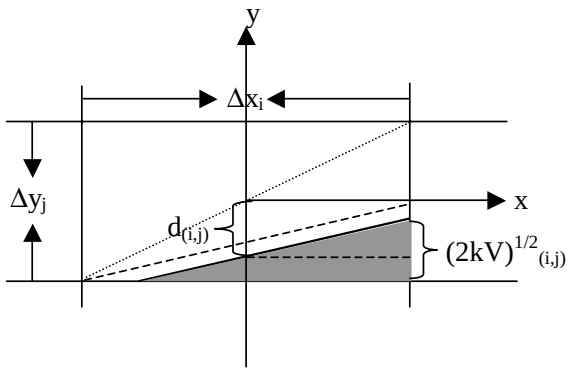

Fig. 2. An example of intersection displacement calculation. The dark area denotes the volume occupied by fluid.

We can improve accuracy by alternating the sweep directions and using more than one sub-cycle (experienced value is about 2–4) in one timestep to update the VOF data. Furthermore, special attention should be paid to the implementation of the algorithm on the originally empty cells that now have fluid after the VOF advection. We need to assign velocity of the newcoming fluid to be equal to the velocity of its donor, not only for the sweep-direction velocity component, but also for the others. Another easy-to-make error will lead to diminished fluid volume. For example, for an empty cell (*i, j*) at *n* timestep, if the liquid enters from its left face in the next timestep, we have $u_{i+1/2,j} - u_{i-1/2,j} < 0$ due to $u_{i+1/2,j} = 0$, making the VOF value calculated from Eq. (20) smaller than it should be. We need to artificially let the velocity difference be equal to zero for these front cells. A simple case – a droplet with an initial velocity moving diagonally in a square domain without gravity, is recommended to check the VOF advection algorithm. An appropriate extrapolation of the velocity field to the outside of a free surface is also a key point for calculating the viscous force, which is extremely important for viscosity dominated flows, such as thin film flows at low Reynolds numbers. The empty cell next to a free-surface cell has the same velocity as the free-surface cell. The one-fluid model is good on the convergence of the Pressure Poisson Equation (PPE) by adjusting coefficients of discretized PPE to give zero pressure for the gas/void cells. A detailed description of the VOF method is available in [23] and in related material of the RIPPLE [19].

For the VOF method based on a fixed rectangular grid, since the free surface is no longer the real computational boundary, the boundary conditions for the computation area become very simple: non-slip boundary condition at the bottom and top wall, continuous condition at the outlet and a given velocity at the inflow. The flow is initiated to be the flat film corresponding to the given *Re*, and the inflow is fixed over the flat film thickness to the same parabolic velocity profile as

$$u_{\text{in}} = \tfrac{3}{2}(2y - y^2)u_{\text{av}}, \tag{24}$$

where u_{av} is the average velocity containing the forcing perturbation as

$$u_{\text{av}} = 1 + \epsilon \sin(2\pi F t). \tag{25}$$

Here, F is the dimensionless forcing frequency and ϵ is the disturbance magnitude. The film running length needs to be quite long to show the development of inlet disturbances. The computation area is 600 or 500 in the x-direction and 2 in the y-direction. The mesh size is 0.4 in x and 0.1 in y. Again the numbers are given in dimensionless units.

The coding and computation are carried out in an IBM AIX environment on an RS/6000 cluster machine. The computation is operated in the serial computing mode, but research into migrating to parallel

computing is in progress. The computation time step is controlled by parameters such as velocity, surface tension, viscosity and mesh size, and encoded in the code. The most time-consuming part is the solving of the PPE, which is done by using the LU factorization solver residing in the ESSL and IMSL math library on the machine.

4. Results and discussion

We choose the vertical ($\beta = 90°$) film configuration in this work under the consideration that regular-pattern waves on vertical films will be well developed in a relatively short distance from the inlet forcing source.

4.1. Small-amplitude waves

The film flow parameters are chosen to be $Re = 20.1$, $We = 33.5$, which corresponds to the experimental case of No. 11 of PLATE 41 reported in the Kapitza study [8]. The parameters are based on the film thickness and average velocity of the flat film, which are determined from the experimentally reported flowrate to be $h_* = 0.183$ mm, $u_* = 10.865$ cm/s, $t_* = 1.684 \times 10^{-3}$ s. Kapitza and Kapitza [8] did not provide the forcing frequency, but reported the steady-state wavelength λ and wave velocity u_w. In our numerical calculation, we obtain the inlet forcing frequency through the relation $F = u_w/\lambda$ from those reported data with the assumption that the waves inherit the frequency of inlet perturbation. The dimensionless forcing frequency is $F = 4.57 \times 10^{-2}$ which corresponds to 27 Hz. The disturbance magnitude ϵ is set to 0.05.

Fig. 3 shows the evolution of the film flow under the inlet forcing perturbation. The small capillary ripples rapidly spread over the whole free surface due to the large surface tension. It is seen that the small capillary waves grow in time, but the wave at the end of exponentially growing region is the largest at the developing stage. Being convective in nature, the waves are transported downstream. In the process, the larger-amplitude waves, due to gravity acceleration, tend to travel faster to catch up with the smaller waves to form even larger ones. It is seen that the biggest one merges with its precursors until it leaves the computational domain. Thereafter, steady-state finite-amplitude waves are established behind. Since at the steady state the waves have nearly the same shape and amplitude, they will travel at nearly the same speed, and no more wave merging processes occurs. We do not see the wave splitting process nor break-up/rupture locations on the film; the film stays continuous. The merging process has been studied experimentally by Liu et al. [2] and numerically by Ramaswamy et al. [16], where the wave interaction is called inelastic one because no repulsion appears as two waves come close to each other. It is often observed that the large one absorbs the slower one.

From the bottom sub-figure of Fig. 3 for the almost steady-state wavy film, we can see that the small disturbance introduced at the inlet experiences a short distance of exponential growth near the inlet. The onset waves behave as predicted by the linear analyses [3] because the forcing frequency is smaller than the cut-off $F_c = 1.53 \times 10^{-1}$. The growth is then arrested by the nonlinear stabilizing effect, and the waves saturate to achieve finite-amplitude stationary periodic waves where the wave shape and wave speed remain unchanged with time and downstream distance. However, they are not exactly stationary; they are nearly stationary. If we perform a close checkup of the picture, we still find (though it is not easy to detect) slightly increasing in wavelength and amplitude, and decreasing in the residual thickness along the nearly stationary periodic wave region. This wave behavior has recently been summarized by Chang [1], and is essentially consistent with the findings by Kapitza and Kapitza [8] and Alekseenko et al. [10] that the mean film thickness decreases as the magnitude of wave motion increases. At the stationary wave regime, the averaged film thickness is 0.945, which compares well with 0.955 given by Alekseenko et al. [10] for the same

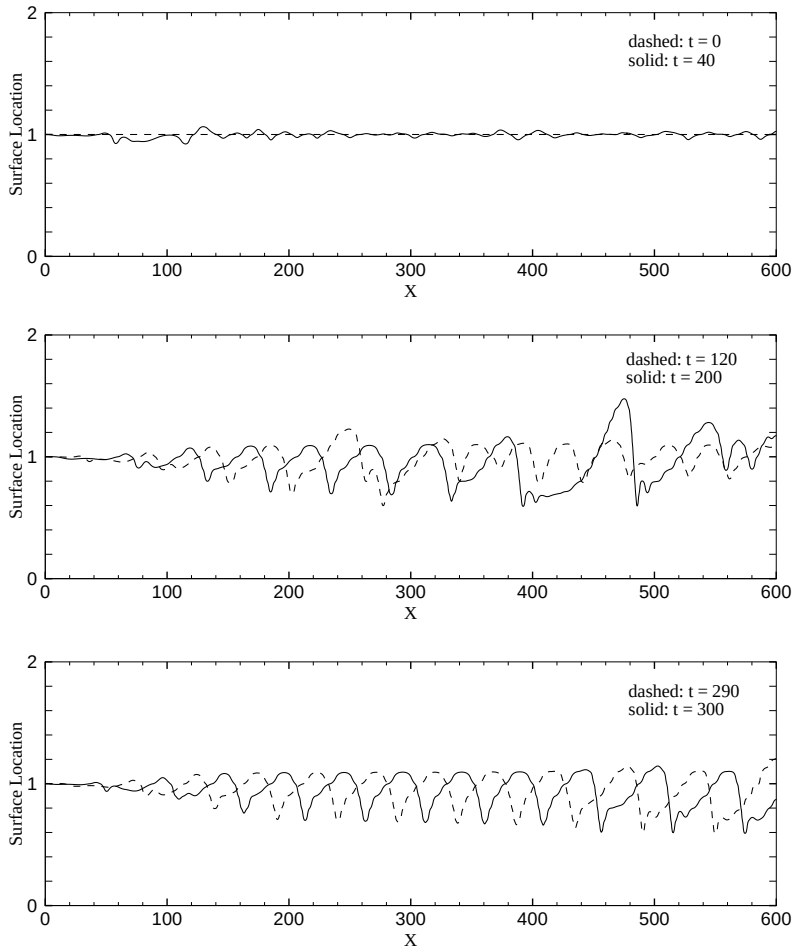

Fig. 3. Instantaneous film thickness for $Re = 20.1$, $We = 33.5$ and $F = 4.57 \times 10^{-2}$.

parameters of $Re = 20.4$ and $\lambda = 48$. But we have to point out the working liquid in Alekseenko et al. is glycerine solution, not water that is used in [8] and in this research. The reduction of film thickness also complies with the reduction by 4% performed by Salamon et al., which led to much better agreement to experimental measurement for wave-velocity.

The calculated wave shape of the almost stationary periodic wave is compared to the shadowgraph provided by Kapitza and Kapitza [8] and the comparison is shown in Fig. 4. The experimental stationary waveform and the numerical one are very similar. The waves appear as a train of nearly sinusoidal-shape waves with a small amplitude. The shape of waves exhibits a slightly steep front and gentle tail. The curvature is large at the wave trough and small at the wave crest and tailing slope. Far downstream from the inlet, we see the waveform deviating from the finite-amplitude sinusoidal type, and a secondary instability (quasi-periodic wave) [2,16] is present. If the plane is sufficiently long, it is expected to see the evolution of sinusoidal waves to large-amplitude solitary waves far downstream as described in [1], and recently verified by Liu and Gollub [2]. Liu et al. [12] gave extensive images (Fig. 13 in [2]) showing that solitary waves can be formed from the evolution of sinusoidal waves along streamwise at the 2-D wave

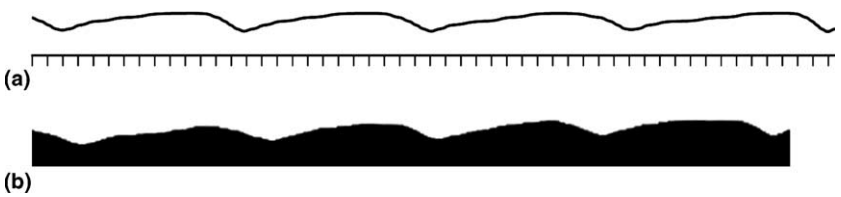

Fig. 4. Comparison of wave shapes taken from (a) simulated result of this work, and (b) Kapitza shadowgraph for $Re = 20.1$, $We = 33.5$ and $F = 4.57 \times 10^{-2}$.

condition. However, as indicated in [12], 2-D small-amplitude waves may develop to be the 3-D before they become solitary waves.

To calculate the wave speed, the view of waveforms at two close moments are magnified and displayed in Fig. 5. The dimensionless wave velocity is 2.2 which is obtained from the separation distance between two trains of waves divided by the time interval. The wave speed of this numerical computation is translated to $u_w = 23.8$ cm/s. Compared with Kapitza's measurement of $u_w = 21.7$ cm/s, this value is acceptable and within the limits of experiments and computations because the VOF method essentially tracks VOF data, reconstructs approximate surfaces and replaces the surface tension force with a body force approximately [24]. However, the result is not as good as the wave velocity $u_w = 22.2$ cm/s reported by Ho and Patera [13] and Salamon et al. [15] using a FEM, where the mean film thickness was conserved, periodic boundary conditions were used, and importantly a Lagrangian-type method (spine) was used to capture the moving surfaces. In the FEMs, the kinematic condition is solved numerically in the mass-conservative form: $\partial h/\partial t + \partial Q/\partial x = 0$, where Q is the flowrate. In periodic boundary conditions, averaging over the domain simply gives $\partial\langle h\rangle/\partial t = 0$ such that the mean film thickness is conserved in time and the flowrate is increased accordingly after the onset of waves [10]. Going back to the experiments where a periodic forcing is applied, the signal is time periodic (in most of the situations) such that averaging over a period gives $\partial\langle Q\rangle/\partial x = 0$ and the mean flowrate is conserved in space. To justify the speculation, Salamon et al. [15] calculated the wavy film flow at the reduced flat film height h_* by 4%, and resulted in the identical wave velocity of $u_w = 21.7$ cm/s. Novertheless, we value the VOF method for such free-surface flow simulations. As summarized by Popinet and Zaleski [25], VOF methods are relatively easy in dealing with large surface deformations, extending to 3-D, and programming. More importantly here, the method can simulate the film flows in experimental conditions.

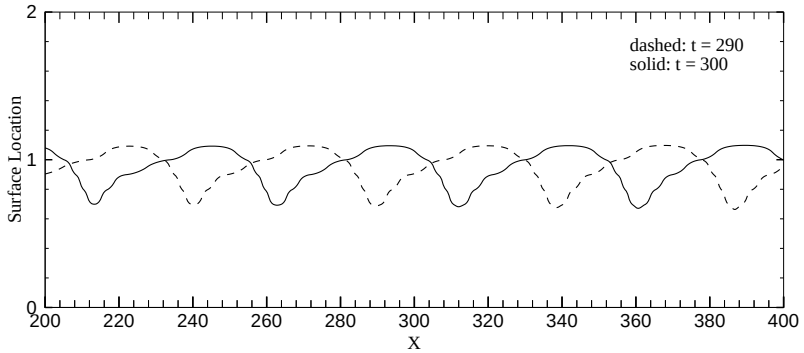

Fig. 5. Two trains of stationary waves for $Re = 20.1$, $We = 33.5$ and $F = 4.57 \times 10^{-2}$.

4.2. Large-amplitude waves

In recent years, Japanese scientist Nosoko et al. [11] reported their experimental observations and measurements of 2-D surface wave dynamics on vertical water films at different forcing frequencies and flowrates. The experimental work covered a wide range of Re (15–90). The traveling wave on the films tends to inherit forcing frequency. They summarized their experimental data and provided a functional dependence of wave velocity on Re, We and wavelength λ, that is,

$$u_w = 1.87We^{-0.06}Re^{-0.293}\lambda^{0.31}. \tag{26}$$

We choose the vertical film with parameters $Re = 69$, $We = 4.2$, and calculated the free surface shapes at the two disturbance frequencies, $F = 4.86 \times 10^{-2}$ and $F = 3.3 \times 10^{-2}$ corresponding to 45 and 30 Hz. The cut-off frequency from Eq. (2) is 4.39×10^{-1}. The disturbance amplitude is $\epsilon = 0.03$ or $\epsilon = 0.05$. We calculated the wavy film perturbed by these two amplitudes at $F = 4.86 \times 10^{-2}$, and we found no difference in wavy characters at the steady state. In fact, all the experiments [2,10,11] reported that the steady-state wave shape is sensitive to the forcing frequency, but insensitive to the forcing strength.

Similar to the previous Kapitza case, after the growing and merging transition stage, the waves saturate to stationary waves downstream. The steady-state wavy surface shapes are shown in Fig. 6 for $F = 4.86 \times 10^{-2}$ and in Fig. 7 for $F = 3.3 \times 10^{-2}$. The waves downstream exhibit strong periodic regularity. The characteristic values of the waves, shape, wavelength, amplitude and phase velocity, remain nearly unchanged, thus they are considered the stationary waves in most theoretical studies. Of course, after close

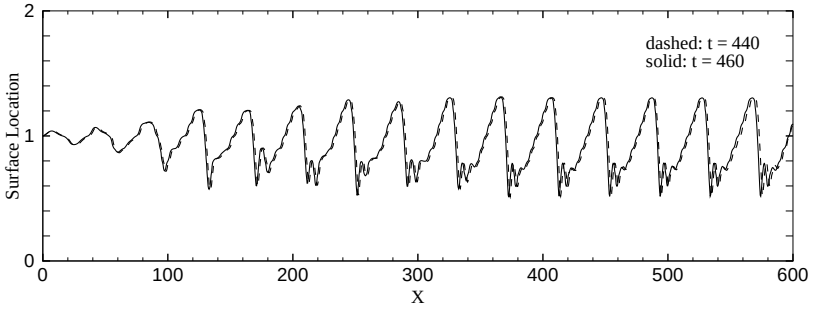

Fig. 6. Steady-state film thickness for $Re = 69$, $We = 4.2$ and $F = 4.86 \times 10^{-2}$.

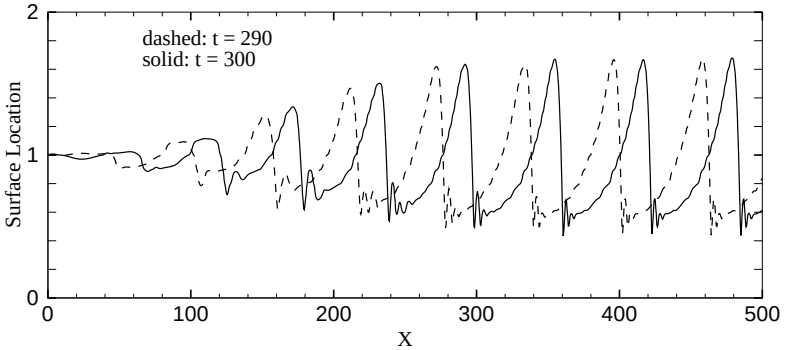

Fig. 7. Steady state film thickness for $Re = 69$, $We = 4.2$ and $F = 3.3 \times 10^{-2}$.

observation and comparison, we perceive the wavelength actually increases slightly with the downstream distance. As we discussed before, this tiny variation may create a problem for simulations using periodic boundary conditions.

In order to estimate the wave velocity, the figures are magnified in x-direction and are focused on the stationary wave region. They are shown in Figs. 8 and 9. For $F = 4.86 \times 10^{-2}$, the wavelength is estimated $\lambda = 40$, and the wave velocity is $u_w = 1.85$. For $F = 3.3 \times 10^{-2}$, the respective values are $\lambda = 62$ and $u_w = 2.0$. Together with the previous simulation result for the Kapitza case, the comparison of simulated wave velocity with Nosoko data summarized in Eq. (26) is plotted in Fig. 10. The results are in good

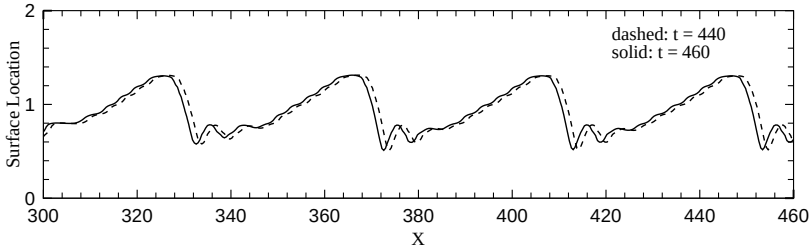

Fig. 8. The stationary waves for $Re = 69$, $We = 4.2$ and $F = 4.86 \times 10^{-2}$.

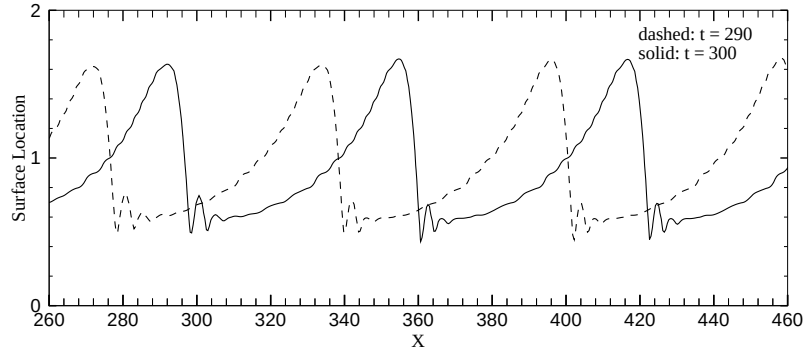

Fig. 9. The stationary wave for $Re = 69$, $We = 4.2$, $F = 3.3 \times 10^{-2}$.

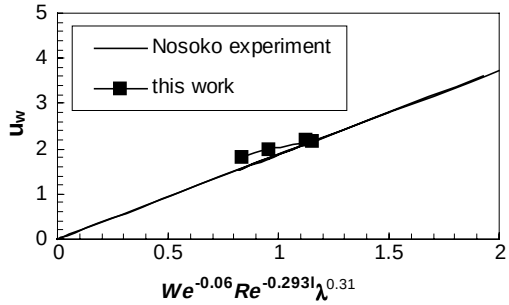

Fig. 10. The comparison of simulated wave velocities with Nosoko et al.'s [11] experimental data.

agreement for the small-amplitude sinusoidal waves, but a little off for the large-amplitude waves at high flowrates.

The above figures also show clearly that the wave shapes are sensitive to forcing frequencies. For the physical and numerical conditions of these two films, the only difference is the forcing frequency. We can see that the inlet perturbation condition prescribes the wave behaviors at a given Re. At low frequency $F = 3.3 \times 10^{-2}$, the stationary wave amplitude and wavelength are much larger than the values at the higher frequency $F = 4.86 \times 10^{-2}$. The tailing edge for wave at $F = 3.3 \times 10^{-2}$ is bent down to form a kind of concave curve, while the tailing edge is nearly an inclined linear line for $F = 4.86 \times 10^{-2}$. The behaviors relative to frequency correspond to those experimental observations [2,10,11]. Compared with the previous Kapitza case, both working frequencies here are much smaller than the cut-off $F_c = 4.39 \times 10^{-1}$, so that the larger-amplitude and more stable waves are formed; whereas in the Kapitza case, the waves near the outlet already display secondary instability. This is qualitatively in agreement with Liu and Gollub [2]. The capillary waves in front of the solitary wave in Fig. 7 have the wavelength of about 4, a little larger than half of the critical wavelength $\lambda_c/2 = 3.4$. Liu and Gollub [2] found that the wavelength of such a fore-runner is about half of λ_c predicted by the linearly stability theory [3].

4.3. Analysis of two different waves

Recalling the Kapitza vertical water (19.6 °C) wavy film shown in Fig. 5 with parameters $Re = 20.1$, $F = 4.57 \times 10^{-2}$ (corresponding to 27 Hz), we recognize the distinct difference from Nosoko's water (23 °C) film of $Re = 69$, $F = 3.3 \times 10^{-2}$ (corresponding to 30 Hz) lies with flowrates. In the case of the high flowrate of Nosoko's film (shown in Fig. 9), a large-amplitude solitary wave is preceded by two small-amplitude capillary bow waves. On the other hand, in the Kapitza case, the small amplitude waves are close to each other and no fore-running capillary waves are generated. The wave shape is a nearly sinusoidal shape with a slightly steeper front and gentle tail. To obtain sinusoidal-type waves on a high flowrate film, the forcing frequency needs to be increased to near the cut-off frequency [2] which precisely increases with the flowrate. However, it is not easy to have stable sinusoidal-type waves; they often manifest quasi-periodic behaviors. Liu and Gollub [2] and Ramaswamy et al. [16] have demonstrated that near the cut-off frequency region, the sideband secondary instability will be more likely to appear rather than sinusoidal-type waves. The qusi-periodic waves already come into sight at the end of flow domain shown in Fig. 3. We have also calculated the case with $Re = 17.23$, $We = 41.06$ and $F = 4.81 \times 10^{-2}$ which has the closer to cut-off frequency than the Kapitza case in Fig. 3. The quasi-periodic waves are very obvious there: double-peak waves appear at the very beginning of evolving path, the amplitudes of both peaks are almost equal, and relative positions of peaks change along streamwise. Note that when the frequency is too high, 3-D instability [12] may first set in before the 2-D waves saturate to a finite-amplitude sinusoidal-type, leading to chaotic surface dynamics.

Figs. 11 and 12 show the velocity vector for about one wavelength of the stationary waves, respectively, for these two films. The vector plots are obtained for the reference coordinates moving with wave velocity $u_w = 2.2$ and $u_w = 2.0$, respectively, for the $Re = 20.1$ case and $Re = 69$ case. For both waves, the velocity field is complicated in the trough region. The strongest variation occurs at the trough in front of the large solitary wave. Inside the large-amplitude wave, as shown in Fig. 12, a large circulation flow is observed; while a circulation is not displayed for the small-amplitude wave shown in Fig. 11. Perhaps this is the reason that large-amplitude stationary waves are often called roll waves. The circulation is restricted in the peak. No circulation is developed at the residual layer. Miyara [26] reported a similar circulation via streamlines at the moving coordinates.

The x-velocity profiles for various parts of the wave are shown in Fig. 13 for the nearly sinusoidal wave and in Fig. 14 for the solitary wave. The velocity profiles are plotted in the dimensionless coordinates (y/h, u/U_{max}) according to normalization by the maximum velocity and film thickness of the respective cross

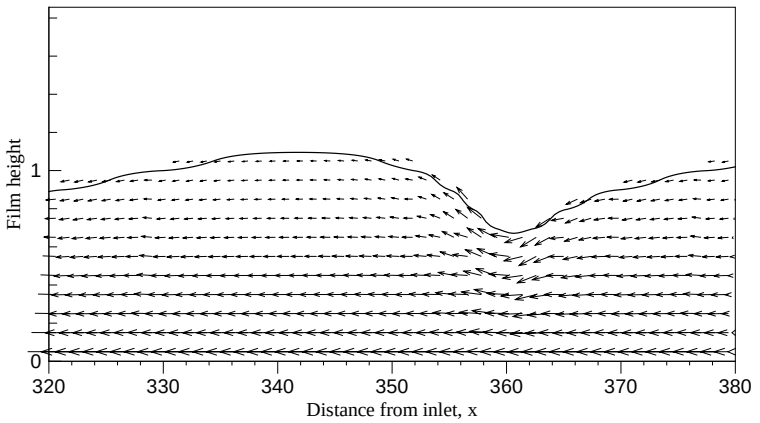

Fig. 11. Velocity vector plot of the nearly sinusoidal wave at the wave-phase moving coordinates for $Re = 20.1$, $We = 33.48$, $F = 4.57 \times 10^{-2}$.

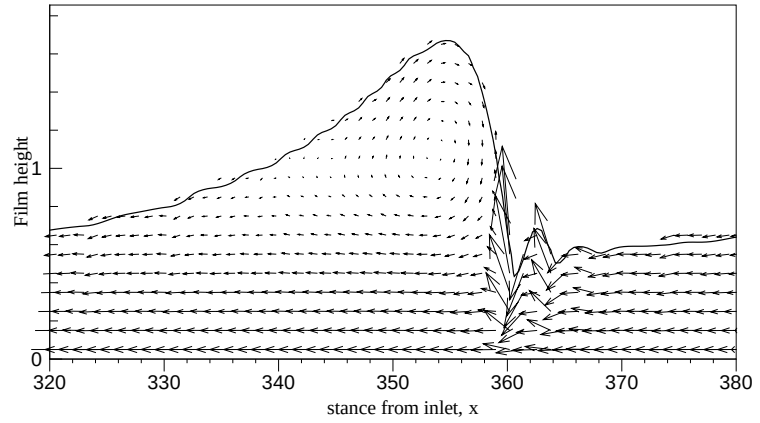

Fig. 12. Velocity vector plot of the solitary wave at the wave-phase moving coordinates for $Re = 69$, $We = 4.2$ and $F = 3.3 \times 10^{-2}$.

sections, so that the velocity profiles at various positions can be drawn in one plot. The positions where the velocity profiles are drawn are indicated and numbered by vertical lines in the legend plot accompanying each velocity profile figure. The solid line in each velocity profile plot designates the parabolic profile for flat films. As seen in the figures, the velocity profile around the crest region and the tailing slope region is very close to the parabolic profile, while at the trough and capillary wave region, the velocity profile undergoes great change with significant variation from the parabolic profile. In Fig. 14, velocity profile 2 bulges over the parabolic line and profile 3 bends down the parabolic line. The intersection of these two profiles points to the existence of circulation flow in the large solitary wave. In contrast, for the nearly sinusoidal wave in Fig. 13, overlaid profiles 2 and 3 indicate the absence of the vortex. The velocity profiles are basically consistent with the Alekseenko et al.'s [10] experimental study as shown in Fig. 15, except that they did not point out the circulation in the big roll. Alekseenko et al. [10] gave the velocity distributions for two characteristic types of waves on a vertical film at $Re = 12.4$. Although the Alekseenko et al. film is not exactly the same as the film we are calculating, Alekseenko et al. [10] implied the dimensionless velocity profile is general to the sinusoidal-type and solitary waves.

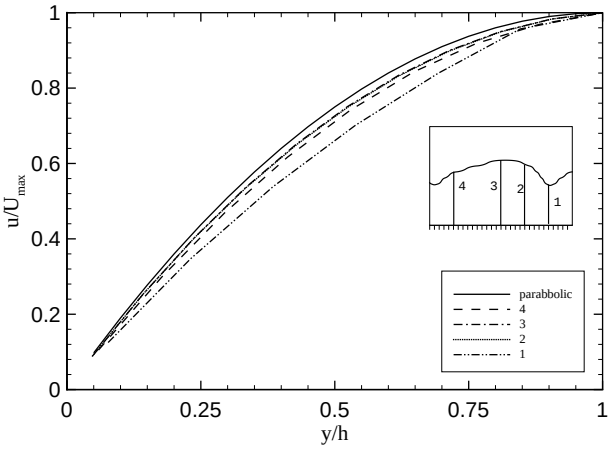

Fig. 13. Velocity profiles along the sinusoidal-type wave.

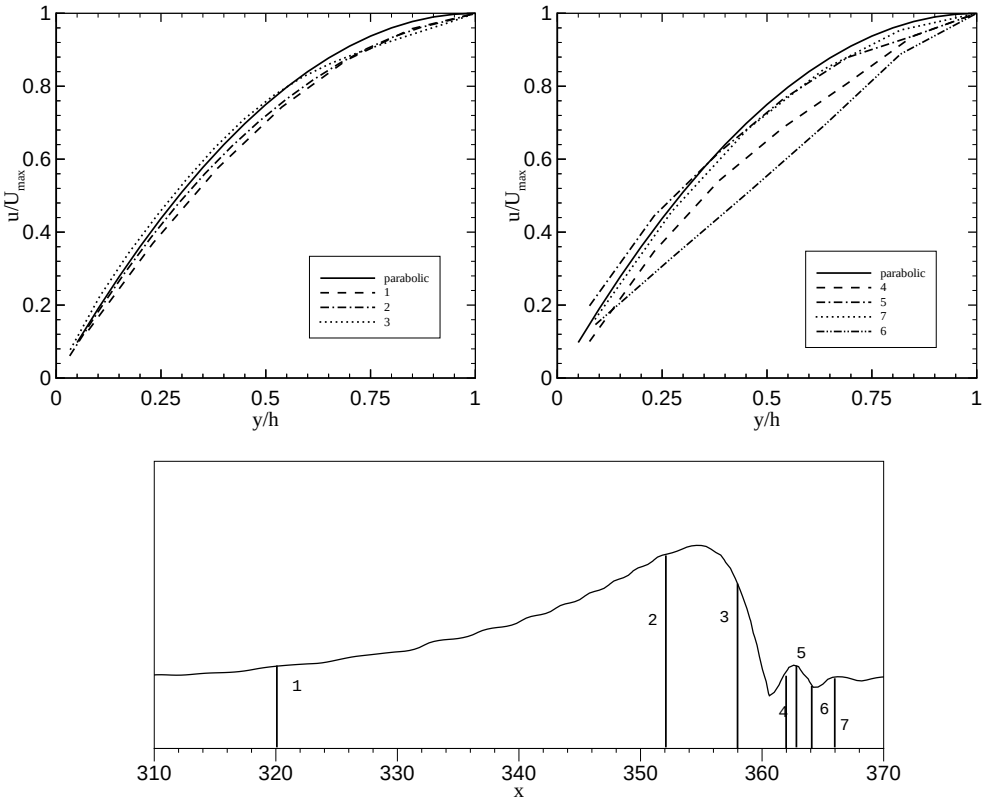

Fig. 14. Velocity profiles along the solitary wave.

The pressure distributions over the range of the x-axis $x = 310 \sim 380$, which covers one stationary wave for both types of waves, are plotted in Figs. 16 and 17. The p_s is the free surface pressure taken from the first 100% filled cell next to the surface and p_w is the pressure next to wall. For the x-positions

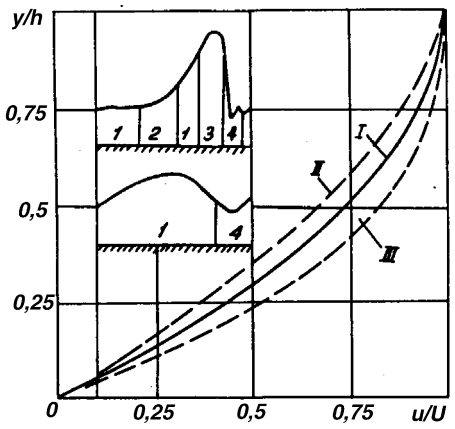

Fig. 15. Velocity profiles along the waves from Alekseenko et al. [10].

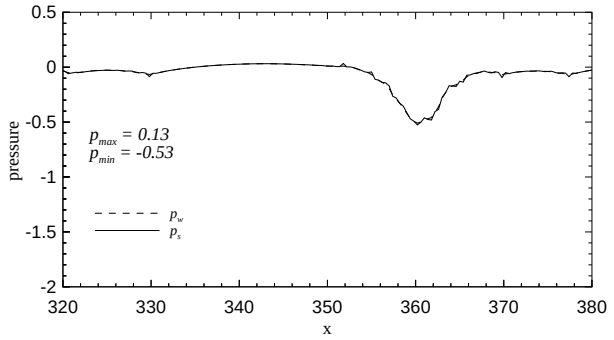

Fig. 16. Pressure distributions at the free surface (p_s) and wall (p_w) along the small-amplitude sinusoidal wave.

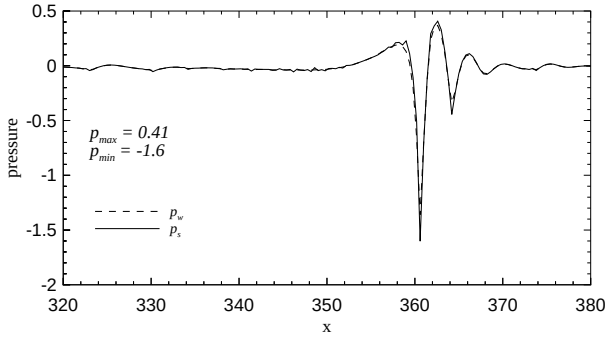

Fig. 17. Pressure distributions at the free surface (p_s) and wall (p_w) along the solitary wave.

relative to the waveforms, please refer to Figs. 5 and 9. In the trough region and capillary wave region where the curvature of the surface is large, the pressure undergoes substantial variation due to the surface tension plus large curvature. The pressure variation at the interface is slightly greater than that at the

wall. In other regions, the pressure distribution is almost equal to zero (the gas pressure), and the difference between surface pressure and wall pressure is negligible. The variation of pressure across film thickness for the large-amplitude solitary wave is greater than for the small-amplitude wave. The difference between surface pressure and wall pressure can be recognized in the figure for solitary waves. At the wave trough in front of the solitary wave, the surface pressure approaches the lowest value $p_s = -1.6$. At the capillary wave region, the pressure distribution also undergoes the oscillation curve corresponding to the surface wave shape.

Periodic boundary conditions are often used to study the nearly stationary waves on thin films [13,15,16]. With the periodic conditions, the computation domain is reduced to one or a few wavelengths, but one can still obtain the wave behaviors after a long time of evolution, so that the computation efficiency is highly improved. The recent computation by Ramaswamy et al. [16] using periodic boundary conditions gave very nice results. Here, we have tried the calculation of Kapitza case with $Re = 20.1$, $We = 33.5$ and $\lambda = 44$ under such periodic conditions, where the film surface is initiated to $h(x, 0) = 1 + 0.02\sin(2\pi x/\lambda)$. The computation domain is four times the wavelength in the x-direction and two times the flat film height in the y-direction. The result is shown in Fig. 18, which clearly shows two distinct wave profiles at $t = 380$. The system does not conserve the stationary traveling waves observed by Kapitza and Kapitza [8] after at least 100 time units, but present quasi-periodic waves instead. Actually, the result is consistent with Fig. 3 obtained by using fixed inlet perturbation, and we already mentioned the quasi-periodic behaviors a few times in previous sections. The quasi-periodic waves appear at the end of evolution course in Fig. 3. The first nearly stationary sinusoidal wave to the last one is about 300 length units apart. Recalling the wave velocity is about 2.2, we estimate that it needs about 136 time units for onset of the quasi-periodic waves. In fact, the two wave profiles were already reported by Ramaswamy et al. [16] (see Figs. 4 and 5 in their paper) in their calculation. They indicated that Kapitza and Kapitza [8] did not observe this type of behaviors because the test section is not long (17 cm) enough for such evolution to emerge. Indeed, Liu and Gollub [2] observed the quasi-periodic waves on their very long test film (200 cm). As far as we have seen, computations using periodic boundary conditions are useful tools to understand secondary instabilities, transitions to other types of periodics or disorder of film flow, which most of the times come into view after long time/long course of wave evolution.

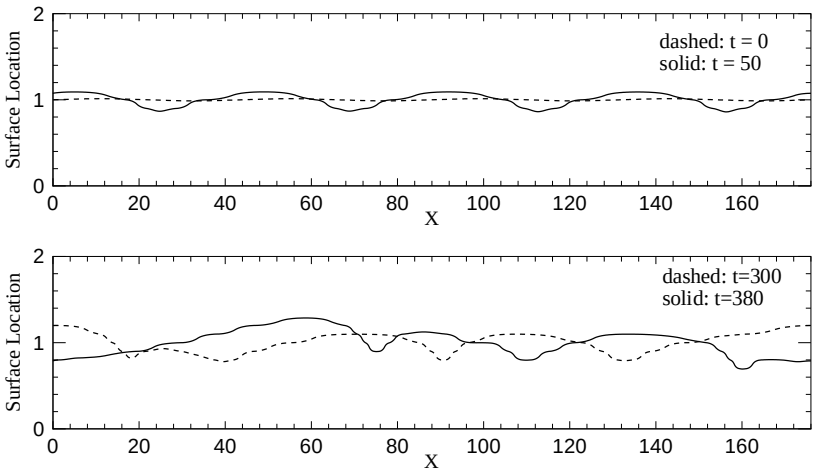

Fig. 18. Simulation result of spatially spread waves under the periodic conditions for $Re = 20.1$, $We = 33.5$ and $\lambda = 44$.

5. Conclusion

Direct numerical simulations of the Navier–Stokes equations using the VOF method have been performed. We have computed surface wave dynamics on vertical thin film flows under a forcing perturbation at the inlet. The computational results are consistent with reported experimental data and numerical studies at various conditions. The parameters affecting wave characteristics are Re, We and disturbance frequency F, and we focus on Re and F. The small forcing perturbation introduced at the inlet experiences an exponential growth and finally achieves a steady nearly-stationary wave state with the wave shape and wave velocity almost unchanged. The nearly stationary waves in fact experience very gradual increases in wavelength and amplitude as they travel downstream due to gravity acceleration, and the phenomenon is more noticeable for the vertical configuration. At low frequency and high flowrate, the small disturbance develops into a solitary wave preceded by small capillary bow waves, and the circulation flow field (in the wave traveling frame) with the size compatible to the solitary wave scale is observed in the solitary wave peak. At high frequency and low Re, the small-amplitude sinusoidal wave without fore-running capillary waves is formed at surface. The quasi-periodic instability is found to accompany the sinusoidal waves. The wave velocity increases with wave separation length and decreases with Re in general. The variation of velocity and pressure are strong at the wave trough and capillary wave region due to the large curvature there. The pressure variation perpendicular to the wall is negligible and only small variations are observed at the solitary wave trough and capillary region. The variation of pressure along the wave propagation direction for the large-amplitude solitary wave is much greater than that for the small-amplitude wave.

The governing equations and the VOF–CSF model for tracking free surfaces and implementing free-surface boundary conditions have been thoroughly described, and the numerical scheme has been applied to the simulation of 2-D thin film flows. The computation using periodic boundary conditions has been tried and the result shows the quasi-periodic wave behaviors in agreement with the conclusions of Ramaswamy et al. [16]. Although the results seem less favorable when compared with other numerical studies [13,15,16] in an FEM, it is worth the effort to place the VOF method into wide applications because it has less constraints. Far downstream from the perturbation source, the nonlinear waves will evolve to be 3-D. Liu et al. [12] have recently done a detailed experimental study of transitional 3-D waves attached to 2-D waves. It is encouraged to extend the 2-D numerical procedure to be able to perform direct simulation of 3-D instabilities, make comparisons with experimental observations and provide further understandings for such thin film instabilities.

Acknowledgements

The authors gratefully acknowledge the support of the US Department of Energy through Grant No. DE-FG03-86ER52123. The first author thanks one of the reviewers very much for his many informative comments, in-depth insights, detailed explanations into this topic, which really improve the author's understanding in physics and numerical methods.

References

[1] H.-C. Chang, Wave evolution on a falling film, Annu. Rev. Fluid Mech. 26 (1994) 103.
[2] J. Liu, J.P. Gollub, Solitary wave dynamics of film flows, Phys. Fluids 6 (1994) 1702.
[3] C.-S. Yih, Stability of liquid flow down an inclined plane, Phys. Fluids 6 (1963) 321.
[4] J. Liu, J.D. Paul, J.P. Gollub, Measurements of the primary instabilities of film flows, J. Fluid Mech. 250 (1993) 69.
[5] B.J. Benney, Long waves in liquid films, J. Math. Phys. 45 (1966) 150.
[6] C. Nakaya, Long waves on a thin fluid layer flowing down an inclined plane, Phys. Fluids 18 (1975) 1407.

[7] H.-C. Chang, Evolution of nonlinear waves on vertical falling films – a normal form analysis, Chem. Eng. Sci. 42 (1987) 515.
[8] P.L. Kapitza, S.P. Kapitza, Wave flow in thin layers of a viscous fluid, in: D. ter Haar (Ed.), Collected Papers of P.L. Kapitza (vol. II), The Macmillan Company, New York, 1964.
[9] W.B. Krantz, S.L. Goren, Stability of thin liquid films flowing down a plane, Ind. Eng. Chem. Fundam. 10 (1971) 91.
[10] S.V. Alekseenko, V.Ye Nakoryakov, B.G. Pokusaev, Wave formation on a vertical falling liquid film, AIChE J. 31 (1985) 1446.
[11] T. Nosoko, P.N. Yoshimura, et al., Characteristics of two-dimensional waves on a falling liquid film, Chem. Eng. Sci. 51 (1996) 725.
[12] J. Liu, J.B. Schneider, J.P. Gollub, Three-dimensional instabilities of film flows, Phys. Fluids 7 (1995) 55.
[13] L.-W. Ho, A.T. Patera, A Legendre spectral element method for simulation of unsteady incompressible viscous free-surface flows, Comput. Methods Appl. Mech. Eng. 80 (1990) 355.
[14] N.T. Malamataris, T.C. Papanastasiou, Unsteady free surface flows on truncated domains, Ind. Eng. Chem. Res. 30 (1991) 2211.
[15] T.R. Salamon, R.C. Armstrong, R.A. Brown, Traveling waves on vertical films: numerical analysis using the finite element method, Phys. Fluids 6 (1994) 2202.
[16] B. Ramaswamy, S. Chippada, S.W. Joo, A full-scale numerical study of interfacial instabilities in thin-film flows, J. Fluid Mech. 325 (1996) 163.
[17] S. Krishnamoorthy, B. Ramaswamy, S.W. Joo, Three-dimensional instabilities in heated falling films: a full-scale direct numerical simulation [Conference Paper], American Society of Mechanical Engineers, Fluids Engineering Division (Publication) FED. v 238, n 3, 1996, ASME, New York, NY, USA, pp. 415–420.
[18] C.W. Hirt, B.D. Nichols, Volume of fluid (VOF) method for the dynamics of free boundaries, J. Comput. Phys. 39 (1981) 202.
[19] D.B. Kothe, R.C. Mjolsness, M.D. Torrey, RIPPLE: A Computer Program for Incompressible Flows with Free Surfaces, LA-12007-MS, Los Alamos National Laboratory, 1991.
[20] W.J. Rider, D.B. Kothe, Reconstructing volume tracking, J. Comput. Phys. 141 (1998) 112.
[21] J.U. Brackbill, D.B. Kothe, C. Zemach, A continnum method for modeling surface tension, J. Comput. Phys. 100 (1992) 335.
[22] E.G. Puckett, A.S. Almgren, J.B. Bell, et al., A high-order projection method for tracking fluid interfaces in variable density incompressible flows, J. Comput. Phys. 130 (1997) 269.
[23] D. Gao, Numerical simulation of surface wave dynamics of liquid metal MHD flow on an inclined plane in a magnetic field with spatial variation, Ph.D. Dissertation, Mechanical Engineering Department, University of California Los Angeles, 2003.
[24] S. Popinet, S. Zaleski, A front-tracking algorithm for accurate representation of surface tension, Int. J. Numer. Mech. Fluids 30 (1999) 775.
[25] R. Scardovelli, S. Zaleski, Direct numerical simulation of free-surface and interfacial flow, Annu. Rev. Fluid Mech. 31 (1999) 567.
[26] A. Miyara, Numerical analysis of a falling liquid film with interfacial waves on an inclined plate, Heat Transfer – Asian Res. 29 (2000) 233.